Structure and phase behavior of a model clay dispersion: A molecular-dynamics investigation

S. Kutter, J.-P. Hansen,[a] and M. Sprik
Department of Chemistry, University of Cambridge, Lensfield Road, Cambridge, CB2 1EW, United Kingdom

E. Boek
Schlumberger Cambridge Research, High Cross, Madingley Road, Cambridge, CB3 0EL, United Kingdom

Reversible molecular-dynamics (MD) simulations have been carried out on simple models for dispersions of circular Laponite clay platelets to investigate the local structure on a mesoscopic scale. The platelets carry discrete charged sites interacting via a screened Coulomb potential. In model A all surface sites have identical negative charge, while model B also includes rim charges of opposite sign. These two models were used in a series of simulations in the semidilute regime, and for three values of the Debye screening length. The structure of the dispersions is characterized by translational and orientational pair distribution functions, and by the corresponding structure factors. Qualitative differences in the pair structure arising from variations in concentration and screening length lead to a tentative identification of sol, gel, and crystal phases. The rim charges have a dramatic effect on the local structure in the strong screening regime, leading to T-shaped pair configuration and clustering of the platelets at low clay concentrations, and at higher concentrations to a space-filling ''house-of-cards'' structure. © *2000 American Institute of Physics.* [S0021-9606(00)70601-5]

I. INTRODUCTION

Our understanding of the structure, phase behavior, and dynamics of colloidal dispersions has progressed enormously in recent years. This progress is mainly due to the availability of well-characterized synthetic samples, the emergence of new experimental techniques, including video microscopy or photon-correlation and two-color spectroscopy, and to the successful application of theoretical tools borrowed from the theory of simple fluids, such as density functional theory DFT.[1] However, most of the experimental and theoretical efforts have focused on monodisperse or polydisperse suspensions of spherical particles, because they lead to obvious simplifications, both in their experimental and theoretical analysis, in particular as regards their effective interactions. As to nonspherical colloidal particles, there is a growing literature on rodlike, natural or synthetic colloids, like the archetypal tobacco mosaic virus (TMV), which lead in particular to lyotropic nematic ordering of entropic origin, as shown already 50 years ago by Onsager.[2]

Clay dispersions, on the other hand, are examples of suspensions of lamellar (or plateletlike) colloidal particles and are the subject of an enormous experimental literature, due to their obvious technological importance in many industrial branches.[3] While the one-dimensional swelling of clays, modeled by stacks of infinite lamellae with intercalated water and counterions, is reasonably well understood theoretically, thanks in particular to detailed molecular simulations,[4,5] there is no clear theoretical picture yet of much more dilute dispersions of finite platelets with more or less random orientations, and in particular of the sol–gel transition. This is partly due to the fact that natural smectite clay particles are highly polydisperse and irregularly shaped.[3] However, the availability of well-characterized synthetic clays, like the disc-shaped Laponite particles, opens up the prospect of a semirealistic statistical description of the structure, phase behavior and rheology of such model clays, the more so since Laponite is being thoroughly explored by a variety of experimental scattering and rheological techniques.[6–10] A statistical description of Laponite dispersions on the mesoscopic scale of the platelet diameter poses a formidable challenge, due to the complexity of the highly anisotropic screened Coulomb interactions between platelets. The simplest situation of a highly swollen, columnar phase of uniformly charged discs may be examined within a Wigner–Seitz cell model, by Poisson–Boltzmann theory.[11] This model is, however, of no help when the platelets are allowed to rotate. A crude model, whereby Laponite platelets and their associated electric double layers are represented by nonintersecting discs carrying a constant electrostatic quadrupole moment, has been investigated by Monte Carlo simulations.[12] The results of these studies point to a reversible sol–gel transition under physical conditions in semiquantitative agreement with experimental data.[8]

The quadrupolar disc model is clearly an oversimplification, which may be criticized on several accounts. In particular it is inadequate at very short range, where any multipolar expansion breaks down, and at long range, where electrostatic interactions between mesoparticles are exponentially screened. In this paper an alternative, more realistic model is

---

[a]Electronic mail: jph32@cus.cam.ac.uk

311

considered, whereby each platelet is characterized by a finite number of discrete charge sites (ν in total) with a fixed surface distribution. The electrostatic potentials are exponentially screened by the microscopic co- and counterions (''microions''), according to linearized Poisson–Boltzmann (PB) theory. The resulting interaction energy between two platelets is the sum of ν^2 site–site screened Coulomb interactions of the Yukawa form. This interaction model may be regarded as a multisite generalization to nonspherical polyions of the classic Derjaguin–Landau–Verwey–Overbeek (DLVO) potential between charge-stabilized spherical colloidal particles.[13] The same multisite picture may be applied to describe interactions between charged rods.[14]

The present paper reports detailed molecular-dynamics (MD) simulations of the local translational and orientational structure of dilute and semidilute dispersions of Laponite platelets based on force fields derived from the above interaction model. The objective is to examine the dependence of the local structure and osmotic properties on Laponite and microion (salt) concentration, and to explore a possible gelation. Recent scattering experiments, combining three radiation sources, are consistent with a complex fractal gel structure spanning several decades in length scale.[10] The present MD simulations are restricted to samples of 32 or 108 platelets, and can hence only probe local structures on the scale of a few disc diameters. On the other hand, the coarse-graining inherent in the model, which integrates out solvent and microion degrees of freedom, implies that the simulations cannot account for the molecular details which are known to control the initial swelling stages.[4] However, the interaction site model adopted in the present work enables us to examine the effect on the local structure of possible rim charges, of opposite sign to the (negative) surface charges carried by the platelets, in a straightforward way. It will be shown in Sec. VI that such rim charges can have a dramatic effect on the local structure in the strong screening (high salt concentration) regime.

II. INTERACTION SITE MODELS

Laponite RD is a synthetic clay, made up of nearly monodisperse, thin cylindrical platelets, with a crystalline unit cell, rather similar to that of the natural montmorilonite phyllosilicates.[15] A typical Laponite platelet has the appearance of a flat coin of diameter $D \approx 25$ nm, thickness $d \approx 1$ nm, and carries a charge of $-0.7e$ per unit cell, amounting to a total surface charge $Q = Ze$ of roughly $Z = -700$. On a supramolecular scale, this charge may be considered as uniformly spread over the total area $\pi D^2/4$ of a two-dimensional disc, corresponding to a uniform surface charge $\sigma = 4Q/(\pi D^2)$. However, because of the lack of spherical symmetry, the bare or screened Coulomb interaction between two uniformly charged platelets is a complicated function of the vector joining their centers and of their orientational degrees of freedom, which can only be reduced to an unwieldy, three-dimensional integral. For that reason, a discrete charge representation was adopted, whereby the total charge Q is distributed over a hexagonal array of ν sites, each site carrying a charge $q = Q/\nu$. The 3 grids of $\nu = 19$, 37, and 61 sites used in the simulations are shown in Fig. 1.
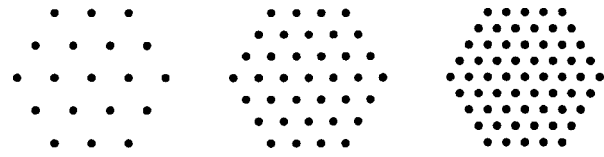

FIG. 1. Hexagonal grids with 19, 37, and 61 charge sites used as model for uniformly charged platelets of radius R.

The corresponding spacing between grid points are $D/4$, $D/6$, and $D/8$, respectively.

In model A, all sites carry identical charges $q = Q/\nu = ze$, with $z = -36.84$, -18.92, and -11.47, respectively. Model B allows for rim charges, by assigning positive charges to the outermost shell of sites, such that the total rim charge amount to 10% of the absolute value of the surface charge, while keeping the total charge of the platelet at the fixed value $-700e$. The resulting distribution of charges is summarized in Table I.

In both models, the suspending fluid (water) is treated as a mere continuum of dielectric constant ϵ ($\epsilon = 78$ for water at room temperature). This assumption is reasonably well justified on the mesoscopic scale, set by the platelet diameter D which far exceeds the correlation length of water. The suspension also contains microions (counterions and added salt), which will screen the Coulomb interactions between sites on different platelets. Let n denote the number of platelets per unit volume, (n_+, z_+) and (n_-, z_-) the concentrations and valences of positive counterions and negative coions. Overall charge neutrality requires that

$$nZ + n_+z_+ + n_-z_- = 0. \tag{2.1}$$

Within linearized PB theory, the effective interactions between charged sites $\mathbf{r}_{i\alpha}$ and $\mathbf{r}_{j\beta}$ on platelets i and j ($1 \leq i, j \leq N$; $1 \leq \alpha, \beta \leq \nu$) are of the DLVO form[13]

$$v_{\alpha\beta}(r) = \frac{z_\alpha z_\beta e^2}{\epsilon r} e^{-\kappa_D r}, \tag{2.2}$$

where $r = |\mathbf{r}_{i\alpha} - \mathbf{r}_{j\beta}|$ and $\kappa_D = 1/\lambda_D$ is the inverse of the Debye screening length of the microions

$$\kappa_D^2 = \frac{4\pi(n_+z_+^2 + n_-z_-^2)e^2}{\epsilon k_B T}. \tag{2.3}$$

A justification of the effective pair potentials (2.2) is given in the Appendix. Two remarks are in order concerning these effective potentials. First, no excluded volume is associated with the interaction between charged sites and microions. Within DLVO theory for spherical colloidal particles, the exclusion of the microions from the colloidal spheres leads

TABLE I. Assignment of site charges for a platelet for which the rim charge is 10% of the face charge and the total charge is $Q = -700e$ (model B).

number of sites	19	37	61
number of rim sites	12	18	24
number of face sites	7	19	37
charge on rim site	6.48	4.32	3.24
charge on face site	−111.11	−40.93	−21.02
spacing between sites [Å]	62.5	41.66	31.25

to an enhancement of the colloid charge by a factor $e^{\kappa_D R}/(1+\kappa_D R)$, where R is the colloid radius. For platelets, the relevant length would be the thickness d, and the resulting factor hardly deviates from 1. In model B, however, the attraction between negative surface charges on one platelet and positive rim charges on another would lead to Coulomb collapse in the simulations. Hence a short-range repulsion must be added to prevent this collapse. For numerical convenience, we have chosen a soft repulsion acting between all sites

$$v_{\text{rep}}(r)=\frac{c}{r^6},\qquad(2.4)$$

where c was taken to be $0.217\cdot10^{-2}$ eV(nm)^6, which yields a repulsive energy of order $k_B T$ at room temperature when the sites are about 0.7 nm apart. This choice is somewhat arbitrary, but convenient for MD purposes. The overall behavior of the model is expected to be insensitive to details of the short-range repulsion.

The second remark is that the mean-field effective potentials completely ignore the specificity of the microions, which only determine the Debye screening length. This coarse graining is acceptable as long as only mesoscopic properties on the scale of the platelet diameter D are considered.

Two characteristics of individual platelets are of interest. Due to inversion symmetry of the discrete charge distribution on a platelet, the electric dipole moment vanishes. Choosing z along the normal to the platelet, the nonzero component of the quadrupole tensor may be expressed as

$$Q_{zz}=\frac{e}{2}\sum_{\alpha=1}^{\nu}\int\rho^{(\alpha)}(\mathbf{r})[3z^2-r^2]d\mathbf{r},\qquad(2.5)$$

where $\rho^{(\alpha)}(\mathbf{r})$ is the charge density associated with site α on the platelet, as defined in Appendix A. Substitution of the explicit form of Eq. (A8) for $\rho^{(\alpha)}(\mathbf{r})$, as obtained within linearized PB theory, into Eq. (2.5) immediately leads to the conclusion that $Q_{zz}=0$. The absence of a quadrupole moment within the present model precludes a direct comparison of the subsequent results with those of Ref. 12.

A second convenient property is the form factor of a single platelet. Let $\mathbf{l}_\alpha$ denote the position of site α with respect to the center of the platelet. The form factor $F(k)$ is defined as:

$$F(k)=\frac{1}{\nu^2}\sum_{\alpha,\beta}\langle e^{i\mathbf{k}\cdot(\mathbf{l}_\alpha-\mathbf{l}_\beta)}\rangle_\Omega=\frac{1}{\nu}+\frac{1}{\nu^2}\sum_{\alpha\neq\beta}\langle e^{i\mathbf{k}\cdot(\mathbf{l}_\alpha-\mathbf{l}_\beta)}\rangle_\Omega,\qquad(2.6)$$

where the average is taken over all orientations $\Omega=(\theta,\phi)$ of the normal to the platelet with respect to the wave vector $\mathbf{k}$. $F(k)$ is easily calculated as a function of k for the three grids of Fig. 1, by sampling orientations from an isotropic distribution of platelet orientations. Results are compared in Fig. 2 to the analytic result corresponding to a disc of radius $R=D/2$ and area $A=\pi R^2$ with a continuous charge distribution. The sum over sites then goes over into an integral over A
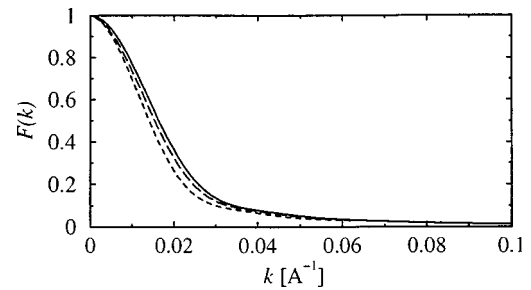

FIG. 2. Form factor for the 19 (short dashed) and 61 (dashed) site models compared to the analytical result for a uniform two-dimensional disc (solid curve).

$$\frac{1}{\nu}\sum_{\alpha=1}^{\nu}e^{i\mathbf{k}\cdot\mathbf{l}_\alpha}\rightarrow\frac{1}{A}\int\int_A e^{i\mathbf{k}\cdot\mathbf{r}}d\mathbf{r},\qquad(2.7)$$

and a straightforward calculation leads to

$$F_R(k)=\frac{2}{k^2R^2}\left[1-\frac{1}{kR}J_1(2kR)\right],\qquad(2.8)$$

where J_1 denotes the cylindrical Bessel function of order 1. Figure 2 shows that in the range $kR\leqslant10$, the results for the 61-site grid are very close to the continuous limit (2.8), while those for 19 sites show reasonably small deviations. The discrete nature of the grids only shows up for $kR>20$, when the amplitude of the form factor has dropped below 0.05. Knowledge of the form factor will be important for the interpretation of the structure factor data in Sec. IV.

III. MOLECULAR-DYNAMICS SIMULATIONS AND DIAGNOSTICS

Model systems consisting of N platelets in a cubic box under periodic boundary conditions were simulated using conventional microcanonical molecular dynamics (MD) methods. The dynamics of the discrete site models A and B, introduced in Sec. II, was solved using the holonomic constraints algorithm of Ciccotti et al.,[16] treating the platelets as completely rigid planar molecules. In this approach a minimum number of mass-carrying basic sites (three for a planar molecule) is selected. These sites form the skeleton of the molecule which is kept fixed by imposing quadratic constraints on the length of the connecting vectors. The remaining sites, which can be massless, are secondary sites and are attached to this frame by fixed linear relations. For the basic sites of the platelets three rim-sites in an equilateral triangular configuration were chosen. These sites were given a mass of 747 900 relative to the proton mass. Secondary sites were left without mass, which implies that the 19, 37, and 61 site models have (almost) identical inertial properties. A typical time step used in the Verlet algorithm for iteration of the (constrained) equations of motion is 20 ps. Apart from infrequent scaling of the velocities at the start of a run, the temperature of a system was not controlled and the trajectories must be considered as essentially sampling the microcanonical ensemble. The screened Coulomb interactions were treated as short range, subject to a spherical cutoff at half the box length. The image vectors are computed from the position of the centers of mass of a pair of platelets and applied

to all sites. After initial equilibration, trajectories were generated and averages taken over 10^4 time steps for the 108-platelet sample, and over $2-5\times10^4$ steps in the case of the smaller 32-platelet system.

Reversible MD ignores the random collisions with the solvent and microions, and the resulting dissipation and hydrodynamic interactions between platelets, so that no physical significance can be associated with the dynamical and transport properties derived from the MD simulations. However, the Brownian and hydrodynamic forces do not affect static properties derived from equal time correlations, implying that such properties may be calculated exactly from MD trajectories, up to statistical uncertainties and finite size effects. Nonetheless, the trajectories were also used to compute some equilibrium time correlation functions to gain some qualitative feeling for the translational and rotational motion of individual platelets under various physical conditions, and in particular in different phases.

A number of diagnostics were used to characterize the simulated samples. Snapshots of instantaneous configurations of the platelets were visualized using three-dimensional computer graphics and the relative motion of the interacting platelets was investigated by animation techniques. Such visualizations, similar to video microscopy now routinely used to observe experimentally prepared samples of micron-size colloidal particles, allow a rapid, qualitative assessment of the local structure and of the possible existence of long range order. Examples will be shown and commented in Sec. V. A more quantitative characterization of the local structure is provided by pair distribution functions. Only site–site distribution functions describing the positional correlations between sites on different platelets were considered. To that purpose, the sites on a platelet were divided into three categories: Category one contains the central site only, coinciding with the center-of mass (CM); category two contains all the sites except the central one and the ones on the periphery of the grid (i.e., the rim sites); and the third category includes only the latter rim sites. This classification allows one to define six different site–site distribution functions $g_{ab}(r)(1 \leq a,b \leq 3)$, but in practice only the CM–CM [$g_{11}(r)$], face–rim [$g_{23}(r)$], and rim–rim [$g_{33}(r)$] functions were considered.

In view of their highly anisotropic shape, orientational correlations between neighboring platelets are expected to be strong, particularly so at high platelet concentrations. Such correlations are characterized by taking the statistical average of the second Legendre polynomial order parameter

$$P(\theta_{ij}) = 3\cos^2(\theta_{ij}) - 1, \tag{3.1}$$

for a fixed distance $r=|\mathbf{R}_i - \mathbf{R}_j|$ between the CM of two platelets. In Eq. (3.1), θ_{ij} is the angle between the normals $\mathbf{n}_i$ and $\mathbf{n}_j$ to platelets i and j. Averaging over all pairs, one arrives at the orientational pair correlation function $g_{or}(r)$. When neighboring platelets are nearly parallel, $g_{or}(r)$ will be positive and close to the maximum allowable value 2, while T-shaped configurations lead to negative values of $g_{or}(r)$.

Equivalently, the local structure can also be characterized in k-space by considering the experimentally accessible structure factor. Let $\mathbf{R}_i$ be the instantaneous CM position of

platelet i, $\mathbf{r}_{i\alpha}$ the position of site α on platelet i, and $\mathbf{l}_{i\alpha} = \mathbf{r}_{i\alpha} - \mathbf{R}_i$ its position relative to the CM. The Fourier components of the microscopic density of sites are

$$\rho_{\mathbf{k}} = \sum_{i=1}^{N}\sum_{\alpha=1}^{\nu} e^{i\mathbf{k}\cdot\mathbf{r}_{i\alpha}} = \sum_{i=1}^{N} e^{i\mathbf{k}\cdot\mathbf{R}_i}\sum_{\alpha=1}^{\nu} e^{i\mathbf{k}\cdot\mathbf{l}_{i\alpha}}. \tag{3.2}$$

The structure factor is defined as

$$S(k) = \frac{1}{N\nu^2}\langle\rho_{\mathbf{k}}\rho_{-\mathbf{k}}\rangle$$
$$= F(k) + S_{\text{inter}}(k), \tag{3.3}$$

where the intramolecular structure factor [corresponding to the $i=j$ self terms in the double sum arising in the first line of Eq. (3.3)] coincides with the form factor introduced in Eq. (2.6), while the intermolecular contribution corresponds to the $i\neq j$ terms. The latter can be expressed in terms of site–site partial structure factors

$$S_{\text{inter}}(k) = \frac{1}{\nu^2}\sum_{\alpha}\sum_{\beta} S_{\alpha\beta}(k). \tag{3.4}$$

The latter are Fourier transforms (FT) of the set of site–site pair distribution functions of which a reduced set [the $g_{ab}(r)$] has been introduced earlier. In particular the CM structure factor

$$S_{\text{CM}}(k) = \frac{1}{N}\sum_{i}\sum_{j}\langle e^{i\mathbf{k}\cdot(\mathbf{R}_i - \mathbf{R}_j)}\rangle, \tag{3.5}$$

is directly related to the FT of $g_{11}(r)$.

If the CM positions and platelet orientations are assumed to be uncorrelated, the intermolecular structure factor factorizes into

$$S_{\text{inter}}(k) = [S_{\text{CM}}(k) - 1]\cdot[f(k)]^2, \tag{3.6}$$

where $f(k)$ is given by the following average over orientations:

$$f(k) = \frac{1}{\nu}\left\langle\sum_{\alpha} e^{i\mathbf{k}\cdot\mathbf{l}_\alpha}\right\rangle_\Omega. \tag{3.7}$$

For a continuous distribution of sites on a circular platelet of radius R

$$f(k) = 4\frac{\sin^2(kR/2)}{(kR)^2}. \tag{3.8}$$

Deviations of MD data from the approximate relation (3.6) provide a measure of the strength of local orientational correlations.

The structure factor also provides a direct link with thermodynamics, via the compressibility relation (valid for ionic fluids[17])

$$\lim_{k\to0} S(k) = \lim_{k\to0} S_{\text{CM}}(k) = nk_BT\chi_T, \tag{3.9}$$

where χ_T is the osmotic compressibility of the suspension.

Translational and rotational temperatures were estimated separately from the kinetic energies associated with the translational motion of the CM and the rotational motion (contributing each $\frac{3}{2}k_BT$ per platelet). In most runs, the mean

temperatures T_t and T_r differ by less than 5%, indicative of good equilibration between translational and rotational degrees of freedom. Occasional larger deviations observed in 32 particle samples are compatible with the small size of the system.

Among other thermodynamic properties, the easiest to compute is the mean potential energy U which follows directly by subtracting the internal kinetic energy from the total energy, or by averaging the instantaneous potential energy

$$V_N = \sum_{i<j} \sum_{\alpha,\beta} v_{\alpha\beta}(|\mathbf{r}_{i\alpha} - \mathbf{r}_{j\beta}|). \qquad (3.10)$$

No attempt was made to compute the osmotic pressure, which cannot be expressed in terms of the site–site pair distribution functions and would require a knowledge of the full molecular pair distribution function. An alternative way of obtaining the osmotic equation of state would be to carry out constant pressure MD simulations.[18]

As already stressed earlier, time-dependent correlation functions and the resulting transport coefficients derived from the MD-generated phase space trajectories are unphysical, since Brownian and hydrodynamic interactions are not included. Nonetheless the CM velocity autocorrelation function (ACF) as well as the mean-square displacement of the CM of the platelets were monitored as functions of time. The resulting self-diffusion constant D yields some qualitative diagnostics of phase behavior, since small or vanishing values of D and an oscillatory behavior of the velocity ACF may be associated with a gel or a crystalline phase.

IV. A TEST OF DISCRETE CHARGE REPRESENTATIONS

Before embarking on large-scale MD simulations of interaction site models for charged platelets, these models were tested in the simpler case of charged colloidal spheres which have been extensively investigated in the past.[19] Due to Gauss' theorem, the Coulomb interaction between two spheres carrying a uniform surface charge σ is identical, for $r>R$, to the potential energy of two point charges placed at the centers, equal to the total charge $Ze = 4\pi R^2 \sigma$ on the surface. Within DLVO theory, the screened Coulomb interaction is then given by Eq. (2.2), with $z_\alpha = z_\beta = Z' = Ze^{\kappa_D R}/(1 + k_D R)$.[13] Accurate simulations[19] and integral equation[20] data are available for the pair structure of this model. Discrete charge representations were tested by carrying out MD simulations for models where ν point charges $z = Z'/\nu$ are regularly distributed over the surface, leading to ν^2 site–site interactions between two spheres. No excluded volume (i.e., hard core) constraint for CM–CM distances less than $2R$ is imposed. Five such regular distributions, summarized in Table II, were considered, and the resulting MD-generated CM pair distribution functions are compared in Fig. 3 to the data of Ref. 19 for uniformly charged spheres for the case $Z=200$, $\lambda_D = 58.9$ nm, $R = 53$ nm $(Z'=259)$ and a packing fraction $\eta = 0.1$. The agreement is seen to be excellent for $\nu = 6, 12, 30, 60$, and ∞ (uniform surface charge); some deviations are observed only in the extreme case ν

TABLE II. Summary of MD simulations for models with discrete charge distributions on the surface of a sphere. N is the total number of spheres, ν the number of sites corresponding to the vertices of regular polyhedra, T is the mean kinetic temperature, and U the mean Coulomb interaction energy. $Z'=259$, $\lambda_D = 58.9$ nm, $R = 53$ nm.

N	ν	T K	U kJ mol^{-1}
108	60	315.6	101.5
108	30	300.4	101.3
108	12	311.5	101.3
108	6	318.7	101.2
108	4	299.5	100.3

$=4$. The slightly enhanced structure in the first peak, observed for the case of a uniform charge is a consequence of the excluded volume constraint. This good agreement holds in a regime where the Debye screening length λ_D is comparable to the particle radius R. As one might expect, the agreement deteriorates somewhat for shorter screening lengths, but only so for the most sparsely distributed sites ($\nu=4$ and 6), when a slight interpenetration of the spheres occurs.

The excellent performance of discrete charge models in the case of spherical charge distributions lends some confidence in the results on platelets, to be discussed in the following sections, particularly in view of the two-dimensional nature of the charged discs.

V. ANALYSIS OF SIMULATION RESULTS

The MD data presented in this section all pertain to model A, involving only identical sites, all of equal charge; results from model B, involving oppositely charged rim sites, will be the subject of Sec. VI.

Simulations were carried out for samples of $N=108$ platelets carrying $\nu=19$ sites each, and for samples with $N=32$ and $\nu=61$ in a cubic simulation box with periodic boundary conditions; some test runs were also made for $\nu=37$ to investigate the ν-dependence of the results, which turned out to remain mostly within statistical errors, as expected from the previous study on charged spheres. Runs were made for three clay concentrations: 1%, 3%, and 5% by weight, and for three screening lengths λ_D. In the limit of vanishing clay concentration, these screening lengths would correspond to monovalent salt concentrations of 10^{-1}, 10^{-2},
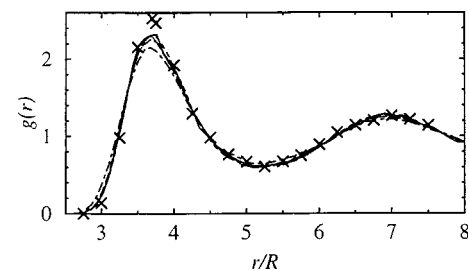

FIG. 3. Center to center pair distribution function $g_c(r)$ for discrete charge models on spheres compared to the result for a continuous charge distribution taken from Ref. 19 (crosses). Indicated are the results for models with the number of sites $\nu=4$ (dash dotted), 6 (long dashed), 12 (short dashed), 30 (thin solid), and 60 (thick solid).

TABLE III. List of MD runs for model A (A1–A11) and B (B1–B6): $\beta U/N$ is the mean potential energy per platelet, divided by the mean thermal energy $(T_t+T_r)/2$.

Run	N	v	w %	$\eta \times 10^{-2}$	λ_D nm	T_t K	T_r K	$\beta U/N$	D 10^{-4} cm^2 s^{-1}
A1	108	19	1	0.4	3.04	301	291	0.37	
A2	108	19	1	0.4	9.6	281	313	171	
A3	108	19	3	1.2	3.04	318	298	3.9	
A4	108	19	3	1.2	9.6	303	301	1510	
A5	108	19	5	2	3.04	316	316	18.4	
A6	32	61	1	0.4	0.96	304	297	0.028	15
A7	32	61	1	0.4	3.04	304	290	0.29	3.7
A8	32	61	3	1.2	0.96	305	325	0.098	3.3
A9	32	61	3	1.2	3.04	287	299	3.3	0.4
A10	32	61	5	2	0.96	293	304	0.21	1.6
A11	32	61	5	2	3.04	298	308	14.4	0.04
B1	32	61	1	0.4	0.96	326	342	−2.26	12
B2	32	61	1	0.4	3.04	288	299	0.21	3.2
B3	32	61	3	1.2	0.96	348	359	−2.15	2.8
B4	32	61	3	1.2	3.04	282	343	1.71	0.8
B5	32	61	5	2	0.96	324	333	−5.28	1.1
B6	32	61	5	2	3.04	335	308	6.4	0.2

and 10^{-3} M. Although the finite thickness of the platelets is not explicitly taken into account in the simulations, one may define the platelet volume $v = \pi R^2 d$ (with $d = 1$ nm) and hence the volume fraction $\eta = nv$; these are listed in Table III, together with other characteristics of the MD runs. Note that the total energies were always adjusted such as to ensure temperatures $T_t \approx T_r \approx 300$ K.

In view of the purely repulsive nature of the effective pair interaction (2.2), the mean potential energy per platelet, as obtained by averaging Eq. (3.10), is always positive. The MD-generated values are listed in Table III. As expected, U increases smoothly with the volume fraction η, and much more sharply with the screening length λ_D, due to the much enhanced range of the repulsion between sites. It should be stressed, however, that U does not coincide with the full excess internal energy of the system, because the effective pair potential (2.2) is temperature-dependent; moreover the co- and counterions, which have been integrated out in the coarse-graining process resulting in Eq. (2.2), lead to a ''volume'' term which would also contribute to the excess internal energy of the suspension.[21]

The most useful information on the suspensions stems from their mesostructure as characterized by the distribution functions and structure factors defined in Sec. III. The insensitivity of the pair structure to the number of sites is illustrated in Fig. 4 which shows CM pair distribution function $g_{11}(r)$ and orientational distribution functions $g_{or}(r)$ as calculated for $v = 19, 37, 61$. The comparison confirms the conclusion of Sec. IV.

With temperature always close to 300 K, four different ''phases'' could be identified upon varying the clay concentration and the screening length λ_D, namely dilute (''gas'') and concentrated (''liquid'') sol phases, as well as gel (or ''glass'') and crystal phases. For the lowest values of η and λ_D, corresponding to low clay concentration and high salt concentration, the suspension behaved as a structureless fluid or gas, which may, loosely speaking, be referred to as a ''dilute sol'' phase. A good example is provided by run No.

A6 in Table III. The corresponding CM pair distribution function $g_{11}(r)$, orientational pair distribution function $g_{or}(r)$ and structure factor are shown in Fig. 5. $g_{11}(r)$ and $S_{inter}(k)$ are featureless, as for an ordinary molecular gas; the same is true of the other site–site functions $g_{23}(r)$ and $g_{33}(r)$ (not shown here). $g_{or}(r)$ indicates preferential parallel orientation of platelets for CM distances of the order of the particle radius or less, as expected. Figure 5(c) also shows the adequacy of approximation Eq. (3.6) in the dilute sol phase. Finally, the velocity ACF decays monotonically, and the resulting self-diffusion constant is high ($D \approx 1.5 \cdot 10^{-3}$ cm^2 s^{-1}); recall, however, that the absolute value of D has no physical meaning, since the Brownian and hydrodynamic forces are ignored in the simulations; only relative values have some physical significance.
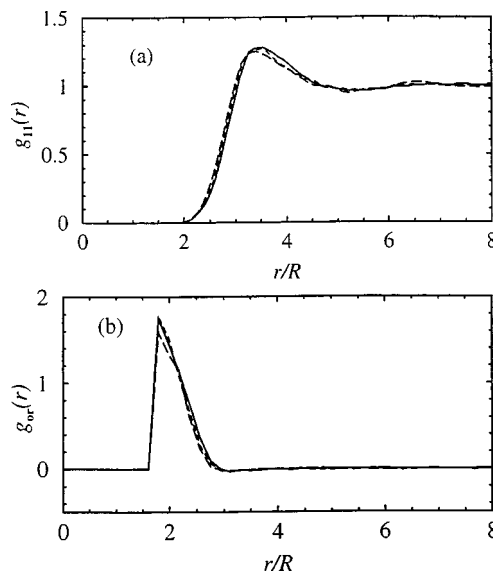

FIG. 4. (a) Site–site radial distribution $g_{11}(r)$ and (b) orientational distribution $g_{or}(r)$ for model A with $v = 19$ (solid), 37 (short dashed), and 61 (long dashed) sites (1% clay and $\lambda_D = 3$ nm).
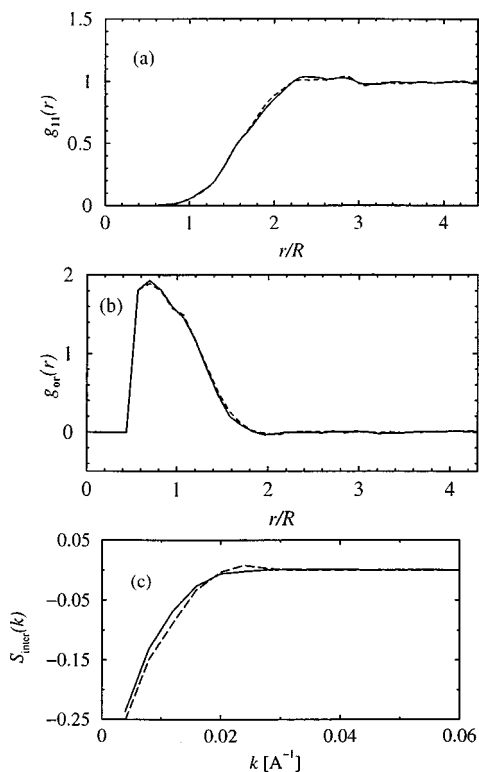
FIG. 5. (a) Site–site radial distribution $g_{11}(r)$, (b) orientational correlation function $g_{or}(r)$ and (c) center-of-mass structure factor $S_{CM}(k)$ for run A6 (see Table III) at 1% clay and $\lambda_D = 0.96$ nm. Dashed and full lines indicate the results after 3×10^4, respectively, 5×10^4 MD steps in (a) and (b). In (c) the dashed line represents approximation (3.6).

pon increasing the clay concentration at constant screening length, the structure gradually builds up, and the diffusion constant drops, as expected, but even at a clay concentration of 5% by weight ($\eta = 0.02$), there is no dramatic change in the pair distribution functions and structure factors; the state may still be regarded as a dilute sol.

The results are much more sensitive to the screening length λ_D. Upon increasing λ_D from 1 to 3 nm at constant clay concentration, the structure is dramatically enhanced, and is reminiscent of that of a simple molecular liquid. A typical configuration of the 32 platelet system is shown in Fig. 6. Pair distribution functions, structure factors and ve-
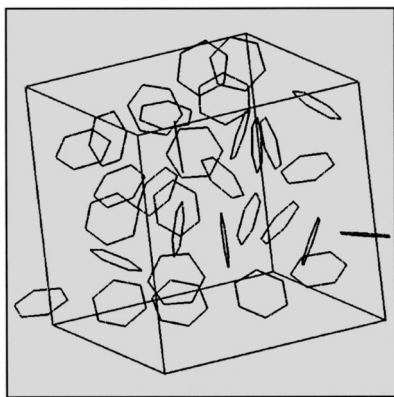

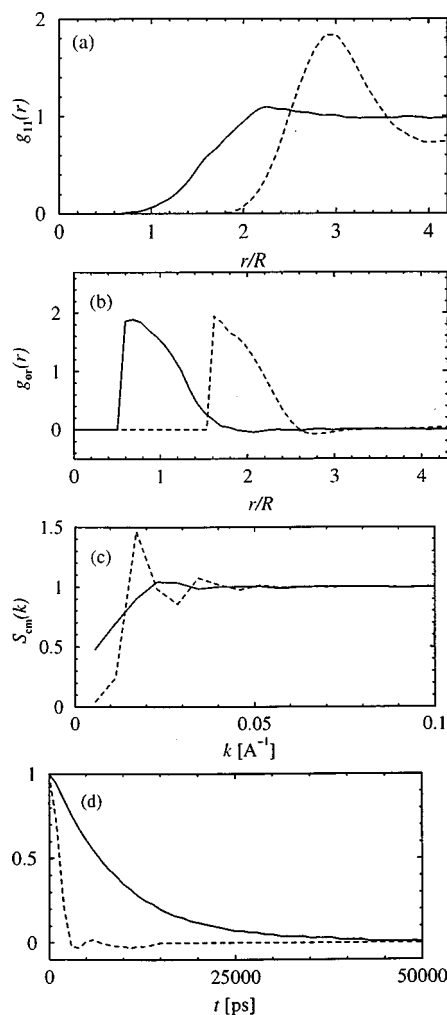FIG. 6. Typical configuration sampled from run A9 for 3% clay, $\lambda_D = 3$ nm.

FIG. 7. (a) $g_{11}(r)$, (b) $g_{or}(r)$, (c) $S_{CM}(k)$, and (d) velocity ACF for model A with 3% clay, and $\lambda_D = 0.96$ nm (solid curves) and $\lambda_D = 3$ nm (dashed curves).

locity ACFs obtained with the two screening lengths for the same clay concentration ($\eta = 0.012$) are compared in Fig. 7. The velocity ACF for $\lambda_D = 3$ nm exhibits a negative dip indicative of caging as observed in simple liquids; the resulting D is reduced by an order of magnitude compared to that observed with the shorter screening length. The highly structured liquid states may be considered as part of a ''concentrated sol'' phase.

For still larger screening length ($\lambda_D = 10$ nm), crystallization of the platelets into an almost perfect fcc (face-centered-cube) lattice was observed with the 108 particle system, upon careful quenching, reheating and re-quenching the sample starting from an initial fluidlike configuration. A typical configuration is shown in Fig. 8. Pair distribution functions and the CM structure factor are plotted in Fig. 9. The CM pair distribution function $g_{11}(r)$ unambiguously points to an fcc crystal. The orientational pair distribution function does not show any significant long range orientational order, so that the crystal of platelets may be regarded as plastic. The velocity ACF exhibits long-lived oscillations resulting from lattice vibrations. The diffusion constant ($D \approx 3 \cdot 10^{-7}$ cm^2 s^{-1}) is orders of magnitude smaller than in the
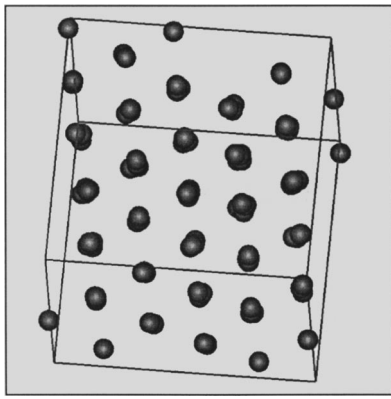
FIG. 8. fcc crystal configurations for run A2 (1% clay, $\lambda_D = 9.6$ nm). Centers of platelets are represented by small spheres nearly aligned along the trigonal crystal axis.

concentrated sol phase. The rms (root mean-square) displacement of the CM of the platelets from their equilibrium lattice sites is about 10% of the nearest neighbor distance, which is typical of molecular crystals close to their melting point (Lindemann criterion).

Crystallization was not always observed in the weak screening regime. At the higher clay concentration, $\eta = 0.012$, the quenching led to a glassy phase, as illustrated in Fig. 10, where the CM pair distribution function differs considerably from its fcc counterpart in Fig. 9; in particular the coordination number in the first shell is about 13, rather than 12. On the other hand, the peaks of the CM structure factor are rapidly damped beyond the first. The self-diffusion con-
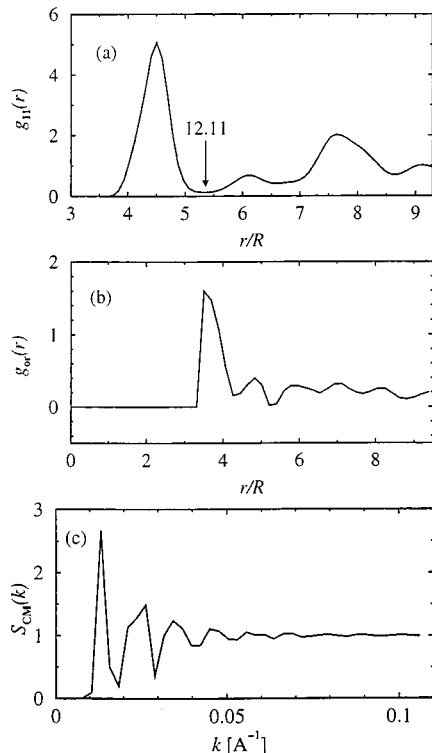

FIG. 9. (a) $g_{11}(r)$, (b) $g_{or}(r)$, and (c) $S_{CM}(k)$ for the crystal state of run A2 (1% clay, $\lambda_D = 9.6$ nm). A coordination number of 12.1 is calculated from Eq. (6.1) with the upper bound r_c indicated by the arrow.
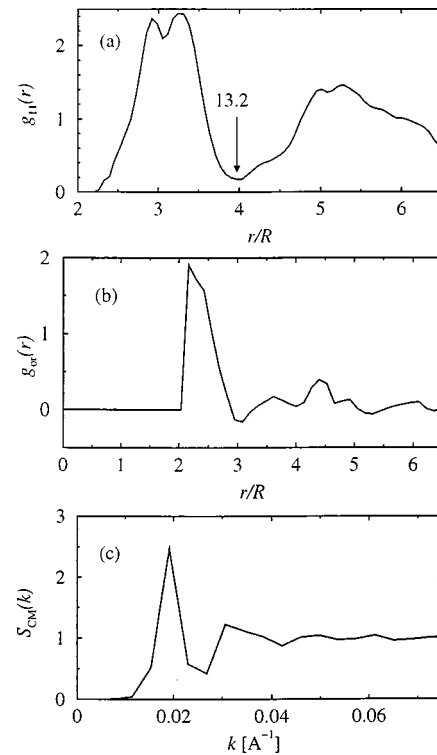

FIG. 10. (a) $g_{11}(r)$, (b) $g_{or}(r)$, and (c) $S_{CM}(k)$ for the glassy state of run A4 (3% clay, $\lambda_D = 9.6$ nm). The arrow points to the radial extension of the coordination shell containing an average number of 13.2 particles.

stant vanishes within statistical uncertainties. Such glassy states may be associated with a gel phase of the clay platelets.

Except under strong screening conditions ($\lambda_D = 1$ nm), corresponding to the ''dilute sol'' phase, the values of the CM structure factors extrapolate to values close to zero in the long wavelength ($k \rightarrow 0$) limit, indicating, according to Eq. (3.9), a very low osmotic compressibility in the concentrated sol, ''gel,'' and crystal phases. The situation will turn out to be quite different when rim charges of opposite sign are included.

VI. EFFECT OF RIM CHARGES

The influence of rim charges on the mesostructure and phase behavior is best understood by comparing the MD results for model B, presented in this section, with those of the previous section pertaining to model A, under similar physical conditions. The first obvious change is apparent from inspection of Table III: The mean potential energy may become negative due to the attraction between positive rim charges and negative surface charges. This attraction dominates the repulsion between surface charges in the strong screening regime. Inspection of typical configurations in this regime, like that shown in Fig. 11, clearly points to the formation of small clusters of platelets which tend to be perpendicular to each other (T-shaped pair configurations). Animation of the platelet trajectories shows that the clusters are relatively long-lived, with the platelets in an initial cluster moving together without loosing contact. Such states will be referred to as ''cluster phase.'' At higher clay concentrations,
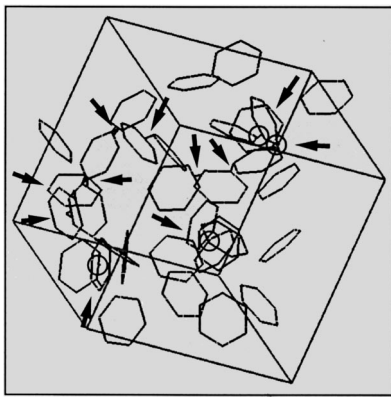
FIG. 11. Typical cluster configuration sampled from run B1 (10% rim charge, 1% clay, $\lambda_D = 0.96$ nm). The arrows point to contacts between platelets.

clusters coalesce into a single house-of-cards-like network,[3] similar to that observed in the simulations of the quadrupolar disc model in Ref. 12 (gel phase). The clustering tends to disappear in the weak screening regime, where the platelets are more uniformly distributed, as in model A where all sites carry charges of the same sign.

These qualitative observations are confirmed by a more quantitative analysis of the pair structure. Figure 12 shows the pair distribution functions in the strong screening regime ($\lambda_D = 1$ nm) for two clay concentrations. The sharp first peak in $g_{11}(r)$ at a distance equal to the platelet radius R confirms the predominance of T-shaped pair configurations at short range. Two features are particularly noteworthy. The small but significant second peak around $r \approx 2R$ is a signature of H-shaped triplet clusters. Secondly, the amplitude of the main peak *drops* as the clay concentration increases; in fact the amplitude drops from a value of about 18 at $\eta = 0.004$ to roughly 6 at $\eta = 0.012$ before re-increasing to about nine at $\eta = 0.02$. While the initial drop reflects a roughly constant nearest-neighbor coordination number

$$\nu_c = 4\pi n \int_0^{r_c} g_{11}(r) r^2 dr, \qquad (6.1)$$

of about 1.5 (with the choice $r_c = 1.5R$), the subsequent increase to about 3.65 signals the coalescence of clusters into a gel-like network. The rim–face and face–face pair distribution functions show considerable structure, reflecting the discrete nature of the site–site model. The structure is damped out at higher clay concentrations. Note the rapid increase of $g_{23}(r)$ close to the origin, due to the strong attraction between oppositely charged rim and face sites. The orientational pair distribution function shows considerably more structure than for model A. The deep negative dip at $r \approx R$ is another clear signature of T-shaped pair configurations.

The corresponding structure factors are plotted in Fig. 13. $S_{CM}(k)$ as well as $S_{inter}(k)$ rise sharply at small k in marked contrast to the liquidlike behavior observed with model A (cf. Fig. 7). According to Eq. (3.9), the peak at $k = 0$ may be associated with a high osmotic compressibility, which in turn signals large concentration fluctuations of the platelets; this enhancement of fluctuations may be traced
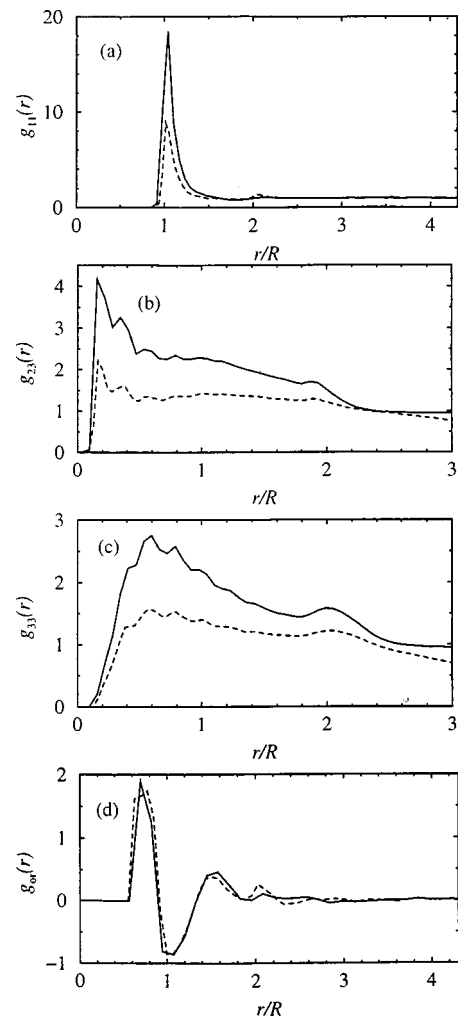

FIG. 12. (a) $g_{11}(r)$, (b) $g_{23}(r)$, (c) $g_{33}(r)$, and (d) $g_{or}(r)$ for run B1 (solid curve, 1% clay) and B5 (dashed curve, 5% clay) both at $\lambda_D = 0.96$ nm. The ripples are not statistical noise but fine structure corresponding to pairs of sites with different locations on the hexagonal grids of Fig. 1.

back to the formation and break-up of clusters and to a gel phase percolating throughout the volume at the higher clay concentration.

The dramatic influence of the opposite rim charges in the strong screening regime is illustrated in Fig. 14 which compares $g_{11}(r)$, $g_{or}(r)$, and $S_{CM}(k)$ under identical conditions ($\eta = 0.012$ and $\lambda_D = 1$ nm) for models A and B. In contrast to the high sensitivity of the pair structure to opposite rim charges, the velocity ACF shows no qualitative change in going from model A to model B, and the resulting diffusion constant D only drops by about 20%.

The effect of the opposite rim charges is, however, considerably weakened for longer screening lengths ($\lambda_D = 3$ nm), corresponding to lower salt concentration. A comparison between the pair structure obtained with $\lambda_D = 1$ and 3 nm is made in Fig. 15. No evidence of T-shaped configurations and clustering is left in the weaker screening regime, where the observed pair structure is hardly distinguishable from that obtained with model A under the same physical conditions. These observations make it clear that a house-of-cards structure would require not only the presence of oppositely charged rim sites, but also strong screening conditions.
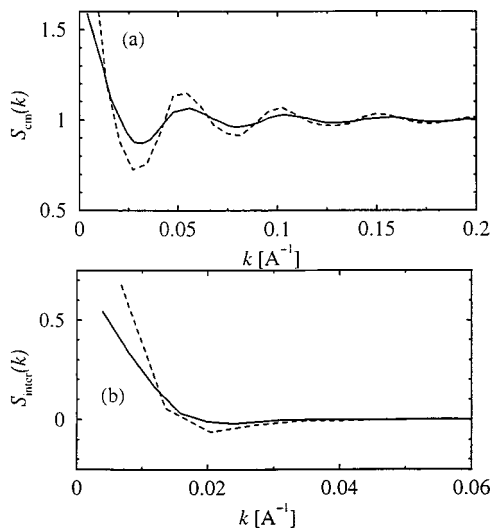
FIG. 13. Structure factors for the same states as in Fig. 12: (a) $S_{CM}(k)$ and (b) $S_{inter}(k)$. Full curves are for 1%, dashed curves for 5% clay.

VII. CONCLUSION

The present exploratory MD investigation of a simple model for the synthetic clay Laponite points to a complex mesostructure and a rich phase behavior, both of which turn out to be very sensitive to clay and salt concentration, and to the presence or absence of rim charges of opposite sign to the surface charges. Upon varying these physical parameters, at least six different phases have been identified, namely dilute and concentrated sol phases (similar to the gas and liquid phases of simple liquids), an fcc crystal phase, a cluster phase and two distinct gel phases. One of these gel phases is
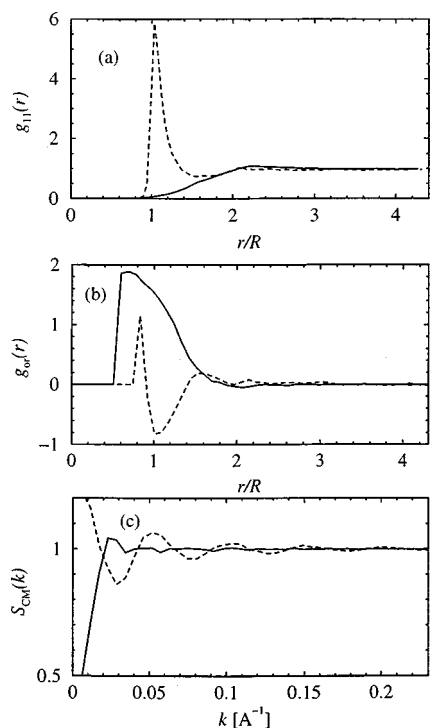

FIG. 14. Comparison between model A (no rim charges, solid curves) and B (10% rim charges, dashed curves) for 3% clay and $\lambda_D = 0.96$ nm; (a) $g_{11}(r)$, (b) $g_{or}(r)$, and (c) $S_{CM}(k)$.

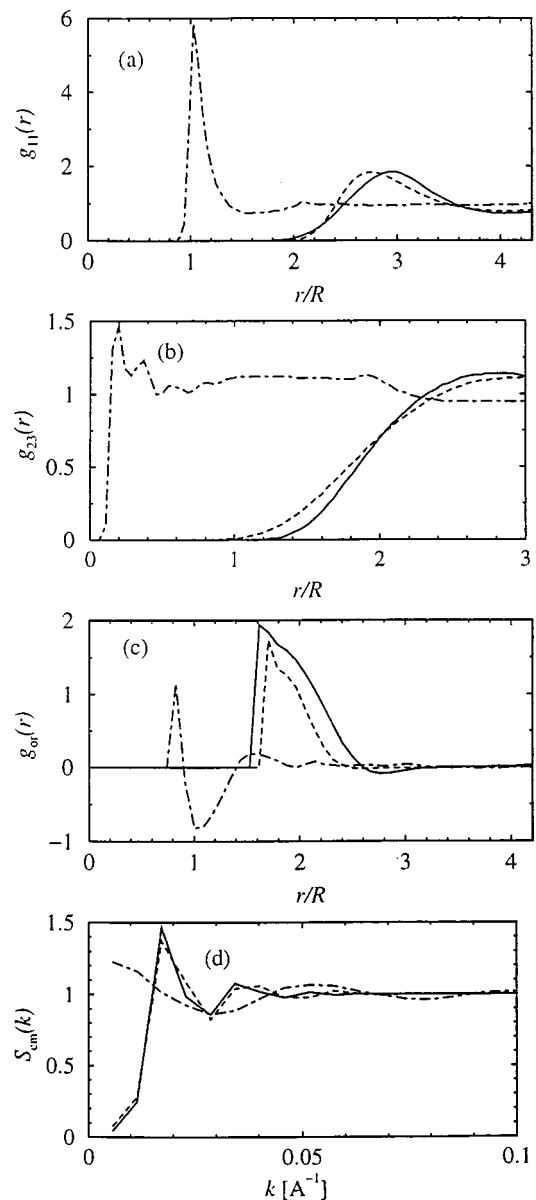FIG. 15. The effect of rim charges at a concentration of 3% clay by weight: (a) $g_{11}(r)$, (b) $g_{23}(r)$, (c) $g_{or}(r)$, and (d) $S_{CM}(k)$. Shown are, for model A, the $\lambda_D = 3$ nm state A9 (solid curves) and for model B, the $\lambda_D = 0.96$ nm (dashed–dotted) and $\lambda_D = 3$ nm (dotted curves) states B3, respectively, B4.

almost certainly metastable with respect to the crystal phase, and is observed when the screening length is of the order of the particle radius, i.e., under strong Coulomb coupling conditions. The second gel phase, on the contrary, is observed under strong screening conditions, when the platelets carry rim charges of opposite sign to the surface charges (model B); the local structure of this second gel phase is of the house-of-cards type. The structural signatures of these various phases are rather clear-cut, but no attempt at a thermodynamic characterization was made. Such a study would require much more extensive simulations of models A and B. In particular, it should be noted that the present exploratory MD simulations were carried out for three fixed values of the Debye screening length. A more systematic investigation of the phase behavior would need to consider the clay and reservoir salt-concentrations as independent thermodynamic

variables, with a corresponding variation of the Debye screening length. Any attempt to determine a complete phase diagram would require accurate determinations of the osmotic free energy of the clay dispersion, including the ''volume term,''alluded to earlier,[21] and which arises when the co- and counterion degrees of freedom are integrated out.

Meanwhile the main conclusion to be drawn from the present simulation work is that positive rim charges lead to considerable short-range orientational ordering and clustering of the negatively charged platelets under strong screening conditions. The existence of positive rim charges is believed to depend strongly on the pH of the suspending fluid.[8,15] In view of the strong structural signature of these rim charges, small angle neutron or x-ray diffraction experiments should be able to discriminate easily between the validity of models A and B to describe clay dispersions.[22] The structural differences between the two models are considerably reduced when the screening length increases (low salt concentration). In the weak screening limit, the behavior of a dispersion of clay platelets turns out to be unexpectedly similar to that of simple fluids.

APPENDIX: EFFECTIVE SITE–SITE PAIR POTENTIALS

Consider a system of N identical rigid polyions (clay platelets in the case under consideration in this paper), each containing ν interaction sites carrying a charge $z_\alpha e (1 \leqslant \alpha \leqslant \nu)$. Let $z_+, \rho_+(\mathbf{r})$ and $z_-, \rho_-(\mathbf{r})$ denote the valences and local densities of the microscopic cations and anions. The local electrostatic potential $\phi(\mathbf{r})$ then satisfies Poisson's equation

$$\nabla^2 \phi(\mathbf{r}) = -\frac{4\pi e}{\epsilon}\left\{ [z_+\rho_+(\mathbf{r}) + z_-\rho_-(\mathbf{r})] \right.$$
$$\left. + \sum_{i=1}^{N} \sum_{\alpha=1}^{\nu} z_\alpha \delta(\mathbf{r}-\mathbf{r}_{i\alpha}) \right\}. \quad (A1)$$

Within mean-field theory, the density profiles $\rho_+(\mathbf{r})$ and $\rho_-(\mathbf{r})$ are replaced by the Boltzmann factors

$$\rho_a(\mathbf{r}) = n_a \exp(-\beta z_a e \phi(r)), \quad a = +, -, \quad (A2)$$

where $\beta = 1/k_B T$; substitution of Eq. (A2) into Eq. (A1) leads to the closed, nonlinear Poisson–Boltzmann (PB) equation for $\phi(\mathbf{r})$. In the spirit of Debye–Hückel–DLVO theory,[13] the Boltzmann factors in Eq. (A2) are linearized, which is strictly speaking valid only in the low charge limit. This results in the linearized PB (LPB) equation

$$(\nabla^2 - \kappa_D^2)\phi(\mathbf{r}) = -\frac{4\pi e}{\epsilon} \sum_{i=1}^{N} \sum_{\alpha=1}^{\nu} z_\alpha \delta(\mathbf{r}-\mathbf{r}_{i\alpha}), \quad (A3)$$

where an unimportant constant has been left out on the right hand side, and κ_D^2 is defined in Eq. (2.3). Equation (A3) is solved by Fourier transformation, resulting in the following linear superposition:

$$\phi(\mathbf{r}) = \sum_i \sum_\alpha \phi_i^{(\alpha)}(\mathbf{r}), \quad (A4)$$

$$\phi_i^{(\alpha)}(\mathbf{r}) = \frac{z_\alpha e}{\epsilon} \frac{e^{-\kappa_D|\mathbf{r}-\mathbf{r}_{i\alpha}|}}{|\mathbf{r}-\mathbf{r}_{i\alpha}|}. \quad (A5)$$

The corresponding charge density of microions

$$e\rho_c(\mathbf{r}) = z_+ e\rho_+(\mathbf{r}) + z_- e\rho_-(\mathbf{r}), \quad (A6)$$

is linearly related to $\phi(\mathbf{r})$, and given by the following superposition:

$$\rho_c(\mathbf{r}) = \sum_i \sum_\alpha \rho_i^{(\alpha)}(\mathbf{r}), \quad (A7)$$

$$\rho_i^{(\alpha)}(\mathbf{r}) = -\frac{z_\alpha \kappa_D^2}{4\pi} \frac{e^{-\kappa_D|\mathbf{r}-\mathbf{r}_{i\alpha}|}}{|\mathbf{r}-\mathbf{r}_{i\alpha}|}, \quad (A8)$$

which obviously satisfies the global charge neutrality condition (2.1) after integration over the total accessible volume V. Equations (A4)–(A8) may then be used to calculate the effective interaction potential between sites (i,α) and (j,β). According to Ref. 23

$$v_{\alpha\beta}(\mathbf{r}_{i\alpha},\mathbf{r}_{j\beta}) = \int z_\alpha e \, \delta(\mathbf{r}-\mathbf{r}_{i\alpha}) \phi_j^{(\beta)}(\mathbf{r}) d\mathbf{r}, \quad (A9)$$

which leads immediately back to the result in Eq. (2.2).

[1] A recent overview of theoretical techniques for fluids is contained, in *New Approaches to Problems in Liquid State Theory*, edited by C. Caccamo, J.-P. Hansen, and G. Stell (Kluwer Academic, Dordrecht, 1999).

[2] L. Onsager, Ann. (N.Y.) Acad. Sci. **51**, 627 (1949); a review of more recent progress is contained in G. J. Vroege and H. N. W. Lekkerkerker, Rep. Prog. Phys. **55**, 1241 (1992)); and in the Doctoral Dissertation of M. van Bruggen (Utrecht, 1998).

[3] See, e.g., H. van Olphen, *Clay Colloid Chemistry*, 2nd ed. (Wiley, New York, 1977).

[4] E. S. Boek, P. V. Coveney, and N. T. Skipper, J. Am. Chem. Soc. **117**, 12608 (1995), and references therein.

[5] A. Delville, J. Phys. Chem. **97**, 9703 (1993).

[6] J. D. F. Ramsay and P. Lindner, J. Chem. Soc., Faraday Trans. **89**, 4207 (1993).

[7] S. D. T. Axford and T. M. Herrington, J. Chem. Soc., Faraday Trans. **90**, 2085 (1994).

[8] A. Mourchid *et al.*, Langmuir **11**, 1942 (1995).

[9] M. Kroon, G. H. Wegdam, and R. Sprik, Europhys. Lett. **35**, 621 (1996).

[10] F. Pignon *et al.*, Phys. Rev. E **56**, 3281 (1997).

[11] E. Trizac and J.-P. Hansen, Phys. Rev. E **56**, 3137 (1997); R. J. F. Leote de Carvalho, E. Trizac, and J.-P. Hansen, Europhys. Lett. **43**, 368 (1998).

[12] M. Dijkstra, J.-P. Hansen, and P. A. Madden, Phys. Rev. E **55**, 3044 (1997).

[13] E. J. W. Verwey and J. T. G. Overbeek, *Theory of Stability of Lyophobic Colloids* (Elsevier, Amsterdam, 1948).

[14] H. Löwen, J. Chem. Phys. **100**, 6738 (1994).

[15] Laporte Inorganics Laponite Technical Bulletin L104/90/A.

[16] G. Ciccotti, M. Ferrario, and J.-P. Ryckaert, Mol. Phys. **47**, 1253 (1982); G. Ciccotti and J.-P. Ryckaert, Comput. Phys. Rep. **4**, 345 (1986).

[17] See, e.g., chapter 10 of J.-P. Hansen and I. R. McDonald, *Theory of Simple Liquids*, 2nd ed. (Academic, London, 1986).

[18] See, e.g., D. Frenkel and B. Smit, *Understanding Molecular Simulation* (Academic, London, 1996).

[19] See, e.g., H. Löwen, J.-P. Hansen, and P. A. Madden, J. Chem. Phys. **98**, 3275 (1993).

[20] J.-P. Hansen and J. B. Hayter, Mol. Phys. **46**, 651 (1982).

[21] M. J. Grimson and M. Silbert, Mol. Phys. **74**, 397 (1991); R. van Roij, M. Dijkstra, and J.-P. Hansen, Phys. Rev. E **59**, 2010 (1999).

[22] An early example of a neutron diffraction study of platelet orientation in neutral montmorrilonite is P. L. Hall *et al.*, J. Chem. Soc., Faraday Trans. 1 **79**, 1687 (1983).

[23] See, e.g., D. Goulding and J.-P. Hansen, Europhys. Lett. **46**, 407 (1999).